Engineering structural diversity in gold nanocrystals by ligand-mediated interface control

Engineering Structural Diversity in Gold Nanocrystals by Ligand-Mediated Interface Control

Yusong Wang,[a,b]* Kadir Sentosun [c], Anran Li [d], Marc Coronado-Puchau [a], Ana Sánchez-Iglesias [a], Shuzhou Li [d], Xiaodi Su [b], Sara Bals [c], Luis M. Liz-Marzán [a,e]*

a) Bionanoplasmonics Laboratory, CIC biomaGUNE, 20009 Donostia-San Sebastián, Spain.

b) Institute of Materials Research and Engineering, Agency for Science, Technology and Research (A*STAR), 3 Research Link, Singapore (117602)

c) EMAT-University of Antwerp, Groenenborgerlaan 171, B-2020, Antwerp, Belgium.

d) School of Materials Science and Engineering, Nanyang Technological University, Singapore.

e) Ikerbasque, Basque Foundation for Science, 48013 Bilbao, Spain.

KEYWORDS: Interface control; Crystal growth; Gold nanocrystals; Surface-enhanced Raman scattering (SERS)

ABSTRACT: Surface and interface control is fundamentally important for crystal growth engineering, catalysis, surface enhanced spectroscopies, and self-assembly, among other processes and applications. Understanding the role of ligands in regulating surface properties of plasmonic metal nanocrystals during growth has received considerable attention. However, the underlying mechanisms and the diverse functionalities of ligands are yet to be fully addressed. In this contribution, we report a systematic study of ligand-mediated interface control in seeded growth of gold nanocrystals, leading to diverse and exotic nanostructures with an improved surface enhanced Raman scattering (SERS) activity. Three dimensional transmission electron microscopy (3D TEM) revealed an intriguing gold shell growth process mediated by the bifunctional ligand 1,4-benzenedithiol (BDT), which leads to a unique crystal growth mechanism as compared to other ligands, and subsequently to the concept of interfacial energy control mechanism. Volmer-Weber growth mode was proposed to be responsible for BDT-mediated seeded growth, favoring the strongest interfacial energy and generating an asymmetric island growth pathway with internal crevices/gaps. This additionally favors incorporation of BDT at the plasmonic nanogaps, thereby

generating strong SERS activity with a maximum efficiency for a core-semishell configuration obtained along seeded growth. Numerical modeling was used to explain this observation. Interestingly, the same strategy can be used to engineer the structural diversity of this system, by using gold nanoparticle seeds with various sizes and shapes, and varying the $[Au^{3+}]/[Au^{0}]$ ratio. This rendered a series of diverse and exotic plasmonic nanohybrids such as semishell-coated gold nanorods, with embedded Raman-active tags and Janus surface with distinct surface functionalities. These would greatly enrich the plasmonic nanostructure toolbox for various studies and applications such as anisotropic nanocrystal engineering, SERS, and high-resolution Raman bioimaging or nanoantenna devices.

INTRODUCTION

Surface and interface control of nanomaterials is fundamentally important for various issues, including crystal growth engineering, catalysis, surface enhanced spectroscopies such as surface enhanced Raman spectroscopy (SERS) and metal enhanced fluorescence (MEF), self-assembly, and colloidal stability. Surface chemistry additionally dictates the interaction of target analytes with solid supports in practical applications including localized electric field (E-field) probing, nanoantenna, fuel cell, solar cell, and SERS-based sensing/imaging among others.[1-5] Understanding the role of ligands in controlling surface properties in plasmonic metal nanocrystal growth has therefore received considerable attention.[6-10] Traditionally, ligand is well-known as capping agent, shape-direct reagent, mediator of reduction kinetics, and even as reducing agent, e.g. in metal crystal growth/engineering for its interaction with the surface of crystal facets, where facets with preferred ligand binding are less exposed and thus grow slower during the metal deposition, as exemplified from different colloidal synthesis such as CTAB-gold NR,[6-7] PVP-silver nanocube,[8] PVP-gold nanostar system.[9] Recently, ligand has been reported to be directly embedded into metal-metal interfaces during the crystal growth for diverse applications, such as the formation of Au decahedra from destabilization of Au_{25} clusters,[11] DNA-embedded core-shell gold

nanoparticles for SERS,[12-13] Raman-tag encoded nanoparticles for multiplex assays,[14] ´BRIGHT´ SERS probe as imaging reagent,[15] and block copolymers-mediated gold particles with Raman tag-encoded nanogap for cancer cells detection.[16] More recently, ligand has been reported to continuously tuning of Au−Ag interfacial strain regulating metal crystal growth pathways resulting in dramatically different morphologies including concentric core−shell, eccentric core−shell, acorn, and dimer structures.[17] However, the underlying mechanisms and the diverse functionalities of ligands are yet to be fully explored.[12-20] Few insights of ligand´s role in the plasmonic nanocrystal growth with solid experimental evidence have been revealed. Mechanistic understanding the role of ligand in metal crystal growth engineering and multi-functionality are thus highly desirable.

We herein report a systematic study of ligand-mediated interface control in plasmonic gold nanocrystals, leading to diverse and exotic nanostructures with an improved activity in surface enhanced Raman scattering (SERS). Three-dimensional analysis based on electron tomography revealed an intriguing gold shell growth process mediated by the bifunctional ligand 1,4-benzenedithiol (BDT), which leads to a unique crystal growth mechanism as compared to other ligands, and subsequently to the concept of interfacial energy control mechanism. The efficiency toward the enhancement of Raman scattering was found to be maximum for a core-semishell configuration obtained by tuning the overgrowth conditions. Numerical modeling was used to explain this observation. Interestingly, the same strategy can be used to engineer the structural diversity of this system, by using gold nanoparticle seeds with various sizes and shapes, and varying the $[Au^{3+}]/[Au^{0}]$ ratio. This generates a series of diverse and exotic plasmonic nanohybrids such as semishell-coated gold nanorods, containing embedded Raman-active tags, which could be used for various applications such as high-resolution Raman bioimaging, or nanoantenna devices, among others.

RESULTS AND DISCUSSION

In our synthetic approach, a coordination complex between Au(I) and cetyltrimethylammonium chloride (Au(I)-CTAC) was selected as the metal precursor in the growth solution while using BDT-modified Au nanocrystals as seeds, with CTAC as stabilizer.[21] As shown by UV-Vis spectroscopy and transmission electron microscopy (TEM in 2D projections and 3D tomography) in Figure 1, the seeded growth mediated by BDT leads to a structural evolution from quasi-spherical Au nanocrystals that were used as seeds and grown at different $[Au^{3+}]/[Au^{0}]$ ratios (R). At a low R value (R = 0.6), a majority of dimer-like nanostrutures were observed (seeds are the bigger components, Figures 1b, S1), which displayed two distinct localized surface plasmon resonance (LSPR) bands (Figure 1a, black curve). The band close to 520 nm can be interpreted as a transverse LSPR, whereas the band around 750 nm can be seen as a longitudinal LSPR. However, when higher R values were used, no low energy bands were present in the spectra and the transverse LSPR was slightly red-shifted (see blue arrows in Figure 1a), corresponding to different nanostructure morphologies including semishells (seeds are the smaller component; R = 2.3) and full shells (R = 11.7) (Figures 1b, S1). Morphological characterization was completed by means of electron tomography reconstructions that allowed us to more clearly recognize different morphologies of the obtained gold nanostructures (Figure 1c). Interestingly, bubble-like regions were consistently found (especially for full shells), indicating the presence of a gap between the seed core and the shell. Such detailed 3D reconstructions obtained by electron tomography allowed us to obtain information on the inner part of the nanostructures (Figure 1d), which clearly revealed the presence of such internal gaps between the BDT-modified seed cores and the grown gold shells. Whereas for R = 0.6 core and shell appear to be in full contact, for R = 2.3 extensive contact but also small nanogaps are found, and for R = 11.7 smaller contact areas and larger nanogaps are present. Further inspection of the 3D reconstructions indicate that the gold shells are not homogeneously coated around the core, i.e. shell growth occurs in a non-conformal manner (Figures S2, S3, S4). Interestingly, previous

examples of similar processes have been reported, such as core-shell gold nanostructures tailored by DNA,[12] but these were found to be the isotropic, even though the size of seeds and overall dimensions are similar to the present case (20 nm, and ~55 nm, respectively). The distinct structural difference highlights the role of ligands in mediating gold shell crystal growth, directing either isotropic or anisotropic growth.

To further understand the ligand-mediated core-shell growth, real-time UV-Vis spectroscopy correlated with TEM was used to monitor the process (Figure S5). Interestingly, a second band emerges in the UV-Vis spectrum at the early stages of reaction, which corresponds to a poorly-defined semishell with small protrusions, partly covering the BDT-modified seed surface. This spectral feature however, gradually evolves into a minor shoulder relative to the main LSPR peak in the final spectrum, similar to the spectral transition reported for DNA-mediated nanostructures.[12] This happens as the semishell transforms into a smooth and rounded nanostructure, resembling the typical morphological changes observed during gold nanostar reshaping.[12-22] Lower Au(I)-CTAC concentrations render a slower kinetics but a clearer view of the LSPR spectral evolution (e.g. the dimer structure) whereas a higher precursor concentration leads to faster kinetics, in which only a single plasmon band is visible (e.g. the full shell structure).[15]

Based on the above observations, we hypothesize that the gold shell growth starts from high energy sites on the BDT-modified gold particle surface, with one or a few initial contact points, then grows into a dimer-like nanostructure, and gradually encapsulates the rest of the BDT-modified seed while becoming smoother, and finally transforms into a semishell or full shell nanostructure, keeping an anisotropic internal structure.

Growth Mechanism

Further insight into the ligand-mediated growth process was obtained by comparing the growth of NPs covered with different ligands, as well as bare NPs. Specifically, bifunctional aromatic ligands, 4-mercaptobenzoic acid (MBA) and 4-aminothiolphenol (ATP), were selected and compared with 1,4-benzenedithiol (BDT) as well as nonfunctionalized seed NPs (No Ligand) as a reference. Interestingly, even though the same reaction conditions were used in all cases, the use of different

ligands resulted in notably different morphologies, as shown in Figures 2 and S6. For a low R of 0.6, the obtained geometries included spheres (for No Ligand), faceted quasi-spheres (for MBA), and core-satellite structures (for ATP), in contrast to the dimer configuration obtained with BDT, which comprises a minimum contact area between the core and the shell. When increasing the R value to 2.3, the BDT-modified seed becomes the smaller part of the dimer nanostructure, clearly indicating continued overgrowth (Figure 1b). For other cases using different ligands, the observed particle morphologies are maintained but with larger features (Figure 2a). Further increasing the R value to 11.7 leads to complete encapsulation of the seed particles in all cases. UV-Vis spectra of the corresponding colloids clearly reflect the observed morphological evolution for increasing R values. The distinct growth pathways observed when using different ligands are the basis to interpret the formation of the different gold nanostructures.

Three principal growth models for the growth of a metal layer on a different metal (either as thin films or core-shell particles) have been reported, namely layered growth (Frank-van der Merwe mode, or FM mode), island growth (Volmer-Weber mode, or VW mode), and an intermediate type (Stanski-Krastanow mode, or SK mode) involving an initial layer-by-layer growth followed by mode island growth [1,2,23] The concept of overall excess energy is used to explain the differences among these growth models, so that a high overall excess energy value would lead to VW mode, an intermediate value to SK mode, and a low value to FW mode. The term of overall excess energy ($\Delta\gamma$) comprises the combination of surface energy (seed, γB), surface energy (shell, γA), strain energy (mainly lattice mismatch between core and shell, $\gamma strain$), and interfacial energy (γi) (see Figure 2C). The key criteria for thin film/core-shell growth is the minimization of the overall excess energy. Since in our system the core and the shell have the same composition, the same surface energy, and no lattice mismatch, the major contribution to overall excess energy should come from the interfacial energy term. Considering that our seeded growth only differs in the selection of ligand, where the different ligands have different binding affinity to gold atoms (-SH > NH2 > -COOH > bare), it could be possible that the ligand binding difference to gold changes the interfacial energy between the core and the shell and then the overall excess energy, which in turn result in different crystal growth

modes. This hypothesis is strongly supported by our experimental observation, where the layer-by-layer mode for No Ligand (FM growth mode with low interfacial energy), the intermediate growth mode for MBA (SK growth mode with medium interfacial energy), and the island growth mode for ATP and BDT (VW growth mode with high interfacial energy) where higher interfacial energy propels the growth system (R = 2.3) to minimize contact area between the core and the shell resulting in a majority of dimer-like nanostructures for BTP but satellite configuration for ATP. In addition, full-shell gold nanostructures under VW growth mode show highly heterogeneous shell coatings (R = 11.7) (Figures 1b,c and 2a). Furthermore, we also found that the ligand incubation conditions affect the growth pathway, meaning that the interfacial energy could be further tuned by ligand density on the seed surface (Figure S7), similar to recent work where 2-mercaptobenzoimidazole-5-carboxylic acid was used as the ligand regulating metal growth.[17]

Considering the above information, we conclude that interfacial energy plays a crucial role in the overgrowth of the second metal, and ligands with different affinity and surface density could be used to tune this term and regulate the seeded-growth pathway in aqueous CTAC solution. Particularly, the BDT-mediated VW growth mode for anisotropic core-shell nanostructures seems to suggest a higher weight of thermodynamic control vs. kinetic control. The concept of interfacial energy control could be applied and used as the growth driving force to explain other experimental observations on the ligand-embedded metal nanostructures in the literature, such as metal– organic layer–metal nanohybrid formation mediated by DNA,[12-14] block copolymers[16] or other small molecules.[15,17] The manipulation of the interfacial energy by ligands may stimulate new synthetic routes in plasmonic metal crystal growth engineering.

Study of Raman Enhancement

Considering that the internal gap inside the core-shell nanoparticles is larger than the BDT molecule dimension as seen from 3D TEM (Figure 1c), VW growth mode with high interfacial energy favors the incorporation of the Raman-active ligand (BDT) into the plasmonic nanogap so that it is embedded between core and shell, meaning that BDT can serve as both interface control agent and Raman probe. The metal-organic layer-metal configuration is also supported by general observation of internal interfaces in TEM images (Figure 1b), which become less sharp upon repeated electron

beam scanning (data not shown). These core-shell nanostructures with internal nanogaps can largely enhance Raman scattering from the ligand because large plasmon-enhanced electromagnetic fields are created precisely at the positions where the Raman-active molecules are located.[24] The SERS response was thus correlated with TEM images, as well as with 3D finite-difference time-domain (FDTD) calculated E-field enhancement maps (Figures 1, 3). Characteristic BDT SERS signals were detected when using three different excitation wavelengths, with the strongest intensity recorded at 785 nm excitation, a lower signal at 633 nm exci-tation, and nearly no response at 532 nm (Figure 3a). The characteristic peaks of BDT at 1057 and 1557 cm^{-1} (Figure S8), were in agreement with previously reported spectra.[25] The SERS response was studied for gold nanostructures obtained using different R values (Figure 3a). At the same particle concentration (based on seed particle number), the maximum SERS intensity (based on the CH bending mode, 1057 cm^{-1}) was obtained from the semishell configuration (R values between 2.3 and 4.7). Even though the dimer configuration has a better LSPR overlap with the 785 nm laser excitation, it was found to yield a lower SERS intensity, which may be due to the smaller size and in particular to a reduced plasmonic gap site, in which fewer molecules are efficiently enhanced. On the other hand, the fully coated particles also display lower SERS intensity than that of the semishell, in spite of containing more available plasmonic nanogap sites. This effect may result from the anisotropy of the semishell configuration, leading to the so-called nanoanntena effect and thus contributing to the overall SERS enhancement.[24,26,27] In the full shell system, this effect may be hindered by losses due to damping through the metal shell.

In addition, the Raman peak position of BDT-mediated nanostructures was also monitored and compared for different samples obtained during shell growth (Figure 3b). With increasing R values, the phenyl ring stretching mode (ca. 1557 cm^{-1}) showed a shift to lower wavenumbers (inset in Figure 3b), which is in accordance with previous [21,25] reports,and related to the orientation-dependent gold surface-BDT phenyl ring π-orbital interaction, (see cartoon illustration in the inset of Figure 3b). All these observations further support that the Raman tag is embedded in the plasmonic core-shell nanostructure, and generates different SERS responses due to local

environmental changes.

In order to better understand this geometry-dependent SERS, 3D finite-difference time-domain (FDTD) simulations were carried out for the dimer, semishell and full-shell configurations (Figure 3c). The average E-field enhancement on the surface of the gold seed for each nanostructure at different excitation wavelengths (532, 633 and 785 nm) is presented in Figure 3c-i. The E-field enhancement under non-polarized incidence was estimated by averaging the E-field enhancements from two simulations with 0° and 90° polarized incidences (Figure S9). Figure 3c-i shows that the dimer exhibits a much smaller E-field enhancement as compared to the other nanostructures under any of the three excitation lines. Interestingly, the most pronounced differences were found at 785 nm excitation, where non-polarized excitation yields ca. two-fold higher E-field enhancement for the semishell than for the full shell. According to the SERS electromagnetic enhancement mechanism, the semishell nanostructure is thus expected to provide 4 times higher SERS intensity than the full-shell nanostructure, in agreement with our SERS experiments (Figure 3a). E-field mappings at 785 nm for both semishell and full-shell were compared (Figure 3c-ii), showing that the full shell yields intense E-fields within the core-shell gap region under either 0° or 90° polarization, originating from strong plasmon coupling within the nanosized gap space. On the other hand, the semishell shows very small E-field enhancement at 0° polarization. However, largely enhanced E-fields are observed in the semishell at 90° polarization within almost the whole core-shell gap region, likely arising from the cooperative interaction of near field coupling and nanoantenna effects. In addition, the higher SERS intensity of the semishell as compared to the fullshell was indeed related to the damping when both the incident and scattered photons pass through the metallic shell. Photon damping in the metallic shell results in a decreased SERS intensity, as exemplified by the shell thickness-dependent E-field enhancement for the full-shell configuration (Figure S10).

Growth of Diverse Gold Nanostructures

Considering that SERS is highly sensitive to the geometry of the plasmonic nanostructures, we extended the ligand-mediated interfacial control strategy to grow diverse gold nanostructures by using gold seeds with different sizes and shapes (Figure 4), including gold nanospheres (20 and 50

nm) and anisotropic nanoparticles resulted in a similar series of dimer, semishell, and fullshell hybrid nanostructures with visible nanogaps for the semishell and full-shell, as seen from HAADF-STEM (nanotriangles and nanorods). Increase in particle size of the spherical BDT-modified seeds from 20 nm to 50 nm images (Figure 4a). The corresponding extinction spectra show gradual changes in correlation with the different nanostructures (Figure 4b). Similar observations were found in the seeded growth using anisotropic nanoparticles including triangular plates and nanorods (Figures 4, S11). Particularly large spectral changes were observed in gold nanorod seeded growth, where the longitudinal LSPR band eventually disappears while the transverse band redshifts and broadens for larger R values. These optical changes were correlated with significant changes in nanostructure morphology as revealed by electron tomography imaging (Figures 4, S11).

When comparing the nanocrystal growth modes for different seeds, we found that the VW island growth model for nanosphere seeded growth appears to apply also to the anisotropic particles. Anisotropic gold nanoparticles show a preference toward growth on surfaces with high curvature, as exemplified by the semishell growth on one end of the nanorods and preferential growth along the edges of nanotriangles (Figures 4a and S11). This minimizes the contact area between core and shell and thus keeps the lowest interfacial energy during shell growth. As a consequence, gold nanorod seeded growth leads to intriguing encapsulation of the nanorod seed starting from just one tip (Figure S11). This effect of the bifunctional ligand to minimize interfacial energy leading to anisotropic nanocrystal growth is significantly different from previously reported ones, involving the use of halides, silver under potential deposition (UPD), or templating surfactant micelles.[28,29] Better understanding surface and interface control would thus provide access to more complex shape control and engineering of noble metal nanocrystals.

The SERS performance of these novel nanostructures was compared using both the analytical enhancement factor (AEF) and the overall SERS intensity at the maximum Raman band from a single nanoparticle entity. Average SERS spectra (from solution) were collected under 785 nm excitation and the most intense SERS band (CH bending mode at 1057 cm^{-1}) was used for comparison (Figure S12). Assuming a closely packed BDT monolayers around the seed nanoparticle

with a footprint of 0.2 nm^2, the AEF was determined by comparing the ratio of the SERS intensity for a given analyte (ISERS) to the corresponding Raman intensity (IRS) under identical experimental conditions, using the following equation: AEF = (ISERS/CSERS)/(IRS/CRS), where CSERS and CRS refer to the analyte concentrations during the SERS and Raman scattering measurements, respectively.[30]

AEF factors were determined for each type of nanostructures, and the maximum AEF values (AEF(max)) are displayed in Table 1, together with the corresponding R values and volume sizes. For instance, cylinder-head gold NR-seeded nanostructures show an AEF from 4.83×10^3 (R = 0) up to 5.90×10^5 (R = 28.7), along with the observed spectral changes (Figure S11). When comparing the maximum AEF of different seed types, nanorods were found to produce the largest enhancement factor (5.90×10^5), followed by 50 nm nanospheres (AEF = 2.16×10^5), nanotriangles (AEF = 1.10×10^5), and 20 nm nanospheres (AEF = 5.14×10^4). The remarkable AEF(max) for BDT-embedded colloidal particles is comparable to other highly active nanoparticle assemblies, such as gold nanotriangle arrays. [31] Furthermore, assuming one BDT molecule rendering one Raman intensity unit, the overall SERS intensity from a single nanoparticle through the ligand-mediated interfacial control has also been given at the maximum SERS enhancement for the different seed types (see Table 1). The nanosphere (50 nm) seed type gives the highest SERS intensity (AEF = 8.49×10^9) with similar order of magnitude as nanorod and nanotrigangle but one order of magnitude higher than nanosphere (20 nm) seed type intensity (AEF = 3.23×10^8). The SERS intensity difference among them is probably due to the difference of localized E-field due to the size and shape-dependent plasmonic coupling besides the plasmonic nanogap. The above information would be very useful and important in single particle Ramanbased applications such as high-resolution cancer cell Raman imaging.

Table 1. SERS performance of plasmonic nanostructures with diverse geometries

Geometry	Nanosphere (20 nm)	Nanosphere (50 nm)	Nanotriangle (60 nm * 20 nm)	Nanorod (46 nm * 12 nm)
$AEF_{(max)}$ (Maximum analytical enhancement factor)	5.14E+04	2.16E+05	1.10E+05	5.90E+05
$I_{(SERS,\ single\ NP)}$ (SERS intensity from a single particle assuming one BDT molecule rendering 1 Raman intensity unit)	3.23E+08	8.49E+09	3.70E+09	5.52E+09
R (Ratio of $[Au^{3+}]/[Au^0]$ at $AEF_{(max)}$)	2.33	0.93	1.81	28.7
Volume of a Single NP (nm^3)	4.19E+03	6.55E+04	3.12E+04	4.78E+03

Notes: 1) BDT is assumed to form a closely packed monolayer around the gold particle seed and has a footprint of 0.2 nm^2. 2) Solution SERS was measured under 785 nm excitation. 3) BDT solution (20 mM) was used as the reference for AEF calculation.

CONCLUSIONS

In summary, we report a systematic study of the seeded growth of plasmonic gold nanocrystals containing internal nanogaps, through ligand-mediated interfacial control with diverse nanostructures. With the aid of electron tomography revealing the internal structure, solid experimental evidence was provided of an intriguing gold shell growth mechanism mediated by BDT, as compared to ligands with different gold-binding affinities, and rationally interpreted with the concept of interfacial energy control mechanism. We conclude that the VW growth mode for BDT-mediated seeded growth favors the strongest interfacial energy, generates an asymmetric island growth pathway with internal crevices/gaps. This additionally favors embedding BDT in the plasmonic nanogaps, and thereby generates strong SERS activity, especially for the semishell configuration. 3D FDTD simulations support the observed geometry-dependent SERS activity. Moreover, the same strategy was employed to engineer the nanocrystal structural diversity by varying gold seed sizes and shapes as well as the $[Au^{3+}]/[Au^0]$ ratio. This rendered a series of exotic plasmonic nanostructures such as semishell-coated gold nanorods, with embedded Raman-active tags and Janus surface with distinct surface functionalities (clean Au surface v.s. ligand-modified one). The demonstrated general strategy to prepare diverse SERS-active plasmonic nanostructures could be readily extended to 1) different plasmonic substrates with ligand-interactive surfaces (e.g. Ag-Ag interface); 2) multicomponent systems (e.g. Au-Ag interface); 3) different bifunctional ligands

for multiplex probe development; and 4) multiple organic-metal interfaces. These would greatly enrich the plasmonic nanostructure toolbox for various studies and applications such as anisotropic nanocrystal engineering, nanoplasmonics, nanoantenna devices, solar cells, SERS, Janus particles,[32] and high-resolution Raman bioimaging, among others.

MATERIALS AND METHODS

Materials. Hydrogen tetrachloroaurate (III) trihydrate ($HAuCl_4 \cdot 3H_2O$, ≥ 99.9%), cetyltrimethylammonium chloride (CTAC), cetyltrimethylammonium bromide (CTAB), sodium borohydride ($NaBH_4$), silver nitrate ($AgNO_3$, ≥ 99.0%), L-ascorbic acid (AA, ≥ 99%), sodium iodide (NaI), 1,4-benzyne dithiol (BDT), 4mercaptobenzoic acid (MBA), 4-Aminothiophenol (ATP), and other chemicals were all purchased from Sigma-Aldrich, and used as received without further purification. Milli-Q water (18.2 MΩ·cm, Millipore) was used in all experiments.

Gold nanoparticle (Au NP) seed preparation and surface functionalization. Au nanospheres (diameter: 20 nm) were prepared by seed-mediated growth with slight modifications.[15] The seeds were made by adding a freshly prepared $NaBH_4$ solution (0.45 mL, 0.01 M) to another solution containing $HAuCl_4$ (0.515 mL, 4.9 mM), CTAC (5 mL, 0.2 M) and Milli-Q (4.5 mL). The growth solution was prepared by adding ascorbic acid (0.15 mL, 0.04 M) to a solution containing $HAuCl_4$ (1.03 mL, 4.9 mM), Milli-Q water (9.0 mL) and CTAC (10 mL, 0.2 M). After aging the seed solution for 1 h, 100 µL seed solution was added into the as-prepared growth solution and left undisturbed overnight. Au nanospheres (diameter: 50 nm) were synthesized via seed-mediated growth.[33] Briefly, initial gold seeds were prepared by reduction of $HAuCl_4$ (5 mL, 0.25 mM) with $NaBH_4$ (0.3 mL, 10 mM) in aqueous CTAB solution (100 mM). An aliquot of initial seed solution (0.11 mL) was added to a growth solution containing CTAC (20 mL, 200 mM), $HAuCl_4$ (20 mL, 0.5 mM) and AA (15 mL, 100 mM), and produce 10 nm gold nanospheres seeds. An aliquot of 10 nm gold nanosphere seeds (0.04 mL) was added to a growth solution containing CTAC (20 mL, 100 mM), and AA (1.3 mL, 10 mM), followed by dropwise addition (2 mL/h) of aqueous $HAuCl_4$ solution (10 mL, 1 mM). This leads to formation of 50 nm monodispersed Au nanospheres. Au nanotriangles (edge/thickness: 60/20 nm) were prepared with a modified protocol.[31] Briefly, the seeds were made by adding a freshly prepared $NaBH_4$ solution (0.3 mL, 0.01 M) to another solution containing $HAuCl_4$ (0.025 mL, 0.05 M) and CTAC (4.7 mL, 0.1 M). The seed was diluted 10 times in 0.1 M CTAC. Then, two growth solutions were prepared: Solution 1) CTAC solution (1.6 mL, 0.1M) was added to Milli-Q water (8 mL), followed by $HAuCl_4$ solution (40 µL, 0.05 M), NaI solution (15 µL, 0.01 M) and ascorbic acid (40

μL, 0.1 M); Solution 2) $HAuCl_4$ solution (500 μL, 0.05 M) was added to CTAC (40 mL, 0.05 M) followed by NaI solution (300 μL, 0.01 M) and ascorbic acid (400 μL, 0.1 M). Subsequently, 100 μL of the seed solution was added to Solution 1, and immediately 3.2 mL of this solution was added to Solution 2. The Au nanotriangle dispersion was left undisturbed at room temperature for 1 h. Finally, the particle dispersion was purified by addition of 6.65 mL of 25 wt % CTAC to Solution 2. The solution was left overnight and the supernatant was removed. The Au nanotriangles at the bottom were then redispersed in CTAC solution. Au nanorods (length/diameter: 46/12 nm) were synthesized by the seed-mediated growth.[34] The seeds were made by adding a freshly prepared, ice-cold aqueous $NaBH_4$ solution (0.6 mL, 0.01 M) to another solution containing $HAuCl_4$ (0.25 mL, 10 mM) and CTAB (7.5 mL, 0.1 M). The growth solution was prepared by adding ascorbic acid (0.32 mL, 0.1 M) to a solution containing $HAuCl_4$ (2 mL, 0.01 M), $AgNO_3$ (0.4 mL, 0.01 M), H_2SO_4 (0.8 mL, 0.5 M), and CTAB (40 mL, 0.1 M). After that, the seed solution (96 μL) was added into the growth solution and left undisturbed overnight. These obtained NP solutions were washed and redispersed in aqueous CTAC solution (5 mM) before further use.

Surface functionalization of Au NP seeds were done by adding bifunctional ligands (BDT, ATP, or MBA) to the as-prepared NP colloid under vigorous mixing, followed by bath sonication for 1 h. A typical functionalization process employed 10 μM ligand incubating with 0.37 nM Au nanosphere (20 nm in diameter) to make sure the excess amount of ligand saturating Au nanoparticle surface (assuming one BDT foot print occupies 0.2 nm^2). Afterwards, the sample solutions were centrifuged twice and washed to remove free ligands in the solution, which is followed by redispersion in aqueous CTAC solution (5 mM) before further use.

Seeded growth of gold nanostructures. The as-prepared ligand-modified Au NPs were used as the seeds for the gold shell growth. Typically, a growth solution containing CTAC, $HAuCl_4$, and AA was first prepared to obtain a transparent solution (complete disappearance of Au^{3+} absorbance peak indicate Au1+ formation). Afterwards, bifunctional ligand-modified Au NP seeds were added into the growth solution while mixing to initiate the seeded growth. The reaction solutions were left undisturbed overnight. After the reaction, the product was centrifuged twice and washed, then

redispersed in CTAC solution (5 mM). The obtained morphology was tuned by changing the R value ($R = [Au^{3+}] / [Au^{0}]$) during synthesis. Kinetic studies were done by recording real-time UV-Vis spectra of the growth solution upon addition of ligand-modified seeds and mixing. Control experiments were also carried out using bare Au NP seeds without bifunctional ligand modification.

Instrumentation and Characterization. UV–vis spectroscopy (Agilent UV–Visible, ChemStation) was used to collect extinction spectra of colloidal solutions. A Raman-IR microscope (Renishaw in Via Raman spectrometer) was used for solution SERS studies under 532, 633, and or 785 nm laser excitation (100% laser power; 10 s exposure time), using ethanol as the calibration sample. Glass vials (Thermo Scientific, National C4015-96, 1 mL clear sepcap vials, 8 × 40 mm) were used for all solution Raman measurements. For each Raman spectrum, the background signal was subtracted. When calculating SERS enhancement factor, pure BDT molecule solution (20 mM in 0.3 M NaOH solution) was used as the reference sample. Note that the SERS response of as-synthesized nanostructures was stable and maintained longer than six months storage at 4 °C. Conventional transmission electron microscopy (TEM) images were obtained using JEOL JEM-2010 (120 kV) or JEM-2100F (200 kV) electron microscopes. TEM sampling was done by drop-casting the particle solution on the TEM copper grids and dried in air.

Electron tomography. Electron tomography experiments were carried out using an FEI Tecnai G2 electron microscope operated at 200kV. A Fischione single tilt tomography holder was employed for the acquisition of the tilt series of 2D projection images. The images for electron tomography tilt series were recorded using high angle annular dark field scanning transmission electron microscopy (HAADF-STEM) with an angular range from -74° to 73° and a tilt increment step of 3°. Alignment of the series was performed using the Inspect 3D software (FEI). Subsequently, the reconstructions were performed using the simultaneous iterative reconstruction technique (SIRT), as implemented in ASTRA Toolbox.[35]

Electric field (E-field) simulation. 3D E-field simulations were performed using a finite-difference time-domain (FDTD) simulation program (FDTD solutions 8.6.3, Lumerical Solutions, Inc., Vancouver, Canada). The parameters for all structures were based on TEM images and extinction

spectra. During all calculations, a total-filed scattered-field source is used to simulate the interaction between propagating waves and metallic nanostructures. The dielectric function of gold was obtained from data provided by Johnson and Christy.[36] External medium was water with a refractive index of 1.33. The gap (1.3 nm) region between gold core and gold shell was assumed to be filled with water. To get accurate results, override mesh regions with 0.25 nm mesh size were used to enclose the whole structure.

ASSOCIATED CONTENT

Supporting Information Additional large-area TEM and electron tomography images, UV-Vis and SERS spectra of various gold nanostructures, and additional FDTD simulations of E-field enhancement for gold nanostructures. This material is available free of charge via the Internet at http://pubs.acs.org.

AUTHOR INFORMATION Corresponding Authors

*E-mail: wangyus@imre.a-star.edu.sg; llizmarzan@cicbiomagune.es

Notes

The authors declare no competing financial interest.

ACKNOWLEDGMENTS

The authors thank Bart Goris for his help with electron tomography. This work was funded by the European Commission (Grant #310445-2, SAVVY). The authors acknowledge financial support from European Research Council (ERC Advanced Grant # 267867-PLASMAQUO, ERC Starting Grant #335078-COLOURATOMS). The authors also appreciate financial support from the European Union under the Seventh Framework Program (Integrated Infrastructure Initiative N. 262348 European Soft Matter Infrastructure, ESMI). Wang Y. and Su X. would like to acknowledge the Agency for Science, Technology and Research (A*STAR), Singapore, for the financial support under the Grant JCO 14302FG096. M. C.-P. acknowledges an FPU scholarship from the Spanish Ministry of Education, Culture and Sports.

REFERENCES

(1) Carbone, L.; Cozzoli, P. D. Colloidal Heterostructured Nanocrystals: Synthesis and Growth Mechanisms. Nano Today **2010**, 5, 449-493.

(2) Peng, Z.; Yang, H. Designer Platinum Nanoparticles: Control of Shape, Composition in Alloy, Nanostructure and Electrocatalytic Property. Nano Today **2009**, 4, 143-164.

(3) Wu, B.; Zheng, N. Surface and Interface Control of Noble Metal Nanocrystals for Catalytic and Electrocatalytic Applications. Nano Today **2013**, 8, 168-197.

(4) Alvarez-Puebla, R. A.; Liz-Marzán, L. M. Traps and Cages for Universal SERS Detection. Chem. Soc. Rev. **2012**, 41, 43-51.

(5) Grzelczak, M.; Liz-Marzán, L. M. Colloidal Nanoplasmonics: From Building Blocks to Sensing Devices. Langmuir **2013**, 29, 4652-4663.

(6) Murphy, C. J.; Thompson, L. B.; Alkilany, A. M.; Sisco, P. N.; Boulos, S. P.; Sivapalan, S. T.; Yang, J. A.; Chernak, D. J.; Huang, J. The Many Faces of Gold Nanorods. J. Phys. Chem. Lett. **2010**, 1, 2867-2875.

(7) Lohse, S. E.; Murphy, C. J. The Quest for Shape Control: A History of Gold Nanorod Synthesis. Chem. Mater. **2013**, 25, 1250-1261.

(8) Rycenga , M.; Cobley, C. M.; Zeng, J.; Li, W.; Moran, C. H.; Zhang, Q.; Qin, D.; Xia, Y. Controlling the Synthesis and Assembly of Silver Nanostructures for Plasmonic Applications. Chem. Rev. **2011**, 111, 3669–3712.

(9) Kumar, P. S.; Pastoriza-Santos, I.; Rodríguez-González, B.; Abajo, F. J. G. d.; Liz-Marzán, L. M. High-Yield Synthesis and Optical Response of Gold Nanostars. Nanotechnology **2008**, 19, 015606.

(10) Ortiz, N.; Skrabalak, S. E. On the Dual Roles of Ligands in the Synthesis of Colloidal Metal Nanostructures. Langmuir **2014**, 30, 6649-6659.

(11) Guan, G.; Liu, S.; Cai, Y.; Low, M.; Bharathi, M. S.; Zhang, S.; Bai, S.; Zhang, Y.-W.; Han, M.-Y. Destabilization of Gold Clusters for Controlled Nanosynthesis: From Clusters to Polyhedra. Adv. Mater. **2014**, 26, 3427–3432

(12) Lim, D. K.; Jeon, K. S.; Hwang, J. H.; Kim, H.; Kwon, S.; Suh, Y. D.; Nam, J. M. Highly Uniform

and Reproducible Surface-Enhanced Raman Scattering from DNA-Tailorable Nanoparticles with 1-nm Interior Gap. Nat. Nanotechnol. **2011**, 6, 452-460.

(13) Oh, J. W.; Lim, D. K.; Kim, G. H.; Suh, Y. D.; Nam, J. M. Thiolated DNA-Based Chemistry and Control in the Structure and Optical Properties of Plasmonic Nanoparticles with Ultrasmall Interior Nanogap. J. Am. Chem. Soc. **2014**, 136, 14052-14059.

(14) Zhao, B.; Shen, J.; Chen, S.; Wang, D.; Li, F.; Mathur, S.; Song, S.; Fan, C. Gold Nanostructures Encoded by Non-Fluorescent Small Molecules in PolyA-Mediated Nanogaps as Universal SERS Nanotags for Recognizing Various Bioactive Molecules. Chem. Sci. **2014**, 5, 4460-4466.

(15) Gandra, N.; Singamaneni, S. Bilayered Raman-Intense Gold Nanostructures with Hidden Tags (Brights) for High-Resolution Bioimaging. Adv. Mater. **2013**, 25, 1022–1027.

(16) Song, J.; Duan, B.; Wang, C.; Zhou, J.; Pu, L.; Fang, Z.; Wang, P.; Lim, T. T.; Duan, H. SERS-encoded nanogapped plasmonic nanoparticles: Growth of metallic nanoshell by templating redox-active polymer brushes. J. Am. Chem. Soc. **2014**, 136, 6838-6841.

(17) Feng, Y.; He, J.; Wang, H.; Tay, Y. Y.; Sun, H.; Zhu, L.; Chen, H. An Unconventional Role of Ligand in Continuously Tuning of Metal-Metal Interfacial Strain. J. Am. Chem. Soc. **2012**, 134, 2004-2007.

(18) Shen, J.; Xu, L.; Wang, C.; Pei, H.; Tai, R.; Song, S.; Huang, Q.; Fan, C.; Chen, G. Dynamic and Quantitative Control of the DNA-Mediated Growth of Gold Plasmonic Nanostructures. Angew. Chem. Int. Ed. **2014**, 53, 8338-8342.

(19) Wang, Z.; Zhang, J.; Ekman, J. M.; Kenis, P. J. A.; Lu, Y. DNA-Mediated Control of Metal Nanoparticle Shape: One-Pot Synthesis and Cellular Uptake of Highly Stable and Functional Gold Nanoflowers. Nano Lett. **2010**, 10, 1886-1891.

(20) Wang, Z.; Tang, L.; Tan, L. H.; Li, J.; Lu, Y. Discovery of the DNA "Genetic Code" for Abiological Gold Nanoparticle Morphologies. Angew. Chem. Int. Ed. **2012**, 51, 9078-9082.

(21) Wang, Y.; Serrano, A. B.; Sentosun, K.; Bals, S.; Liz-Marzán,

L. M. Stabilization and Encapsulation of Gold Nanostars Mediated by Dithiols. Small **2015**, 11,

4314-4320.

(22) Rodriguez-Lorenzo, L.; Romo-Herrera, J. M.; Perez-Juste, J.; Alvarez-Puebla, R. A.; Liz-Marzan, L. M. Reshaping and LSPR Tuning of Au Nanostars in the Presence of CTAB. J. Mater. Chem. **2011**, 21, 11544-11549.

(23) Bauer, E.; Van Der Merwe, J. H. Structure and Growth of Crystalline Superlattices: From Monolayer to Superlattice. Phys. Rev. B **1986**, 33, 3657-3671.

(24) Shiohara, A.; Wang, Y.; Liz-Marzán, L. Recent Approaches toward Creation of Hot Spots for SERS Detection. J. Photochem. Photobiol. C **2014**, 21, 2–25.

(25) Joo, S. W.; Han, S. W.; Kim, K. Adsorption of 1,4Benzenedithiol on Gold and Silver Surfaces: Surface-Enhanced Raman Scattering Study. J. Colloid Interface Sci. **2001**, 240, 391-399.

(26) Alvarez-Puebla, R.; Liz-Marzán, L. M.; García de Abajo, F. J. Light Concentration at the Nanometer Scale. J. Phys. Chem. Lett. **2010**, 1, 2428-2434.

(27) Alvarez-Puebla, R. A.; Agarwal, A.; Manna, P.; Khanal, B. P.; Aldeanueva-Potel, P.; Carbó-Argibay, E.; Pazos-Pérez, N.; Vigderman, L.; Zubarev, E. R.; Kotov, N. A.; Liz-Marzán, L. M. Gold Nanorods 3D-Supercrystals as Surface Enhanced Raman Scattering Spectroscopy Substrates for the Rapid Detection of Scrambled Prions. Proc. Nat. Acad. Sci. **2011**, 108, 8157-8161.

(28) Personick, M. L.; Mirkin, C. A. Making Sense of the Mayhem Behind Shape Control in the Synthesis of Gold Nanoparticles. J. Am. Chem. Soc. **2013**, 135, 18238-18247.

(29) Lohse, S. E.; Burrows, N. D.; Scarabelli, L.; Liz-Marzán, L. M.; Murphy, C. J. Anisotropic Noble Metal Nanocrystal Growth: The Role of Halides. Chem. Mater. **2014**, 26, 34-43.

(30) Le Ru, E. C.; Blackie, E.; Meyer, M.; Etchegoin, P. G. Surface Enhanced Raman Scattering Enhancement Factors: A Comprehensive Study. J. Phys. Chem. C **2007**, 111, 13794–13803.

(31) Scarabelli, L.; Coronado-Puchau, M.; Giner-Casares, J. J.; Langer, J.; Liz-Marzán, L. M. Monodisperse Gold Nanotriangles: Size Control, Large-Scale Self-Assembly, and Performance in Surface-Enhanced Raman Scattering. ACS Nano **2014**, 8, 5833-5842.

(32) Rodríguez-Fernández, D.; Liz-Marzán, L. M. Metallic Janus and Patchy Particles. Part. Part. Syst. Charact. **2013**, 30, 46-60.

(33) Zheng, Y.; Zhong, X.; Li, Z.; Xia, Y. Successive, Seed-Mediated Growth for the Synthesis of Single-Crystal Gold Nanospheres with Uniform Diameters Controlled in the Range of 5–150 nm. Part. Part. Syst. Charact. **2014**, 31, 266–273.

(34) Wang, Y.; Aili, D.; Selegård, R.; Tay, Y.; Baltzer, L.; Zhang, H.; Liedberg, B. Specific Functionalization of CTAB Stabilized Anisotropic Gold Nanoparticles with Polypeptides for Folding-Mediated Self-Assembly. J. Mater. Chem. **2012**, 22, 20368-20373.

(35) Van Aarle, W.; Jan Palenstijn, W.; De Beenhouwer, J.; Altantzis, T.; Bals, S.; Joost Batenburg, K.; Sijbers, J. The ASTRA Toolbox: A Platform for Advanced Algorithm Development in Electron Tomography. Ultramicroscopy **2015**, 157, 35–47.

(36) Johnson, P. B.; Christy, R. W. Optical constants of the noble metals. Phys. Rev. B **1972**, 6, 4370-4379.

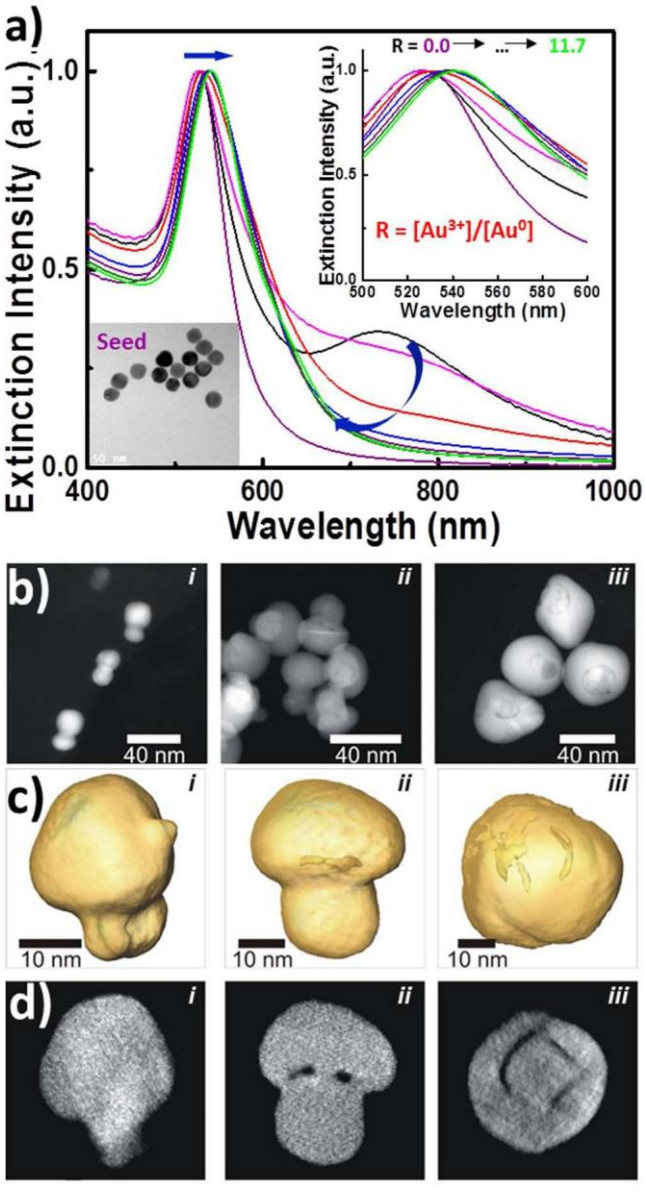

Figure 1. Evolution of quasi-spherical gold nanocrystals during BDT-mediated seeded growth. a) UV-Vis spectra (the inset is a TEM image of the seeds). b) HAADF-STEM images of samples with varying $[Au^{3+}]/[Au^{0}]$ ratios (R): (i) 0.6, (ii) 2.3, (iii) 11.7. c,d) Electron tomography reconstructions and slices through the reconstructed internal structure, of single gold nanostructures at different growth stages.

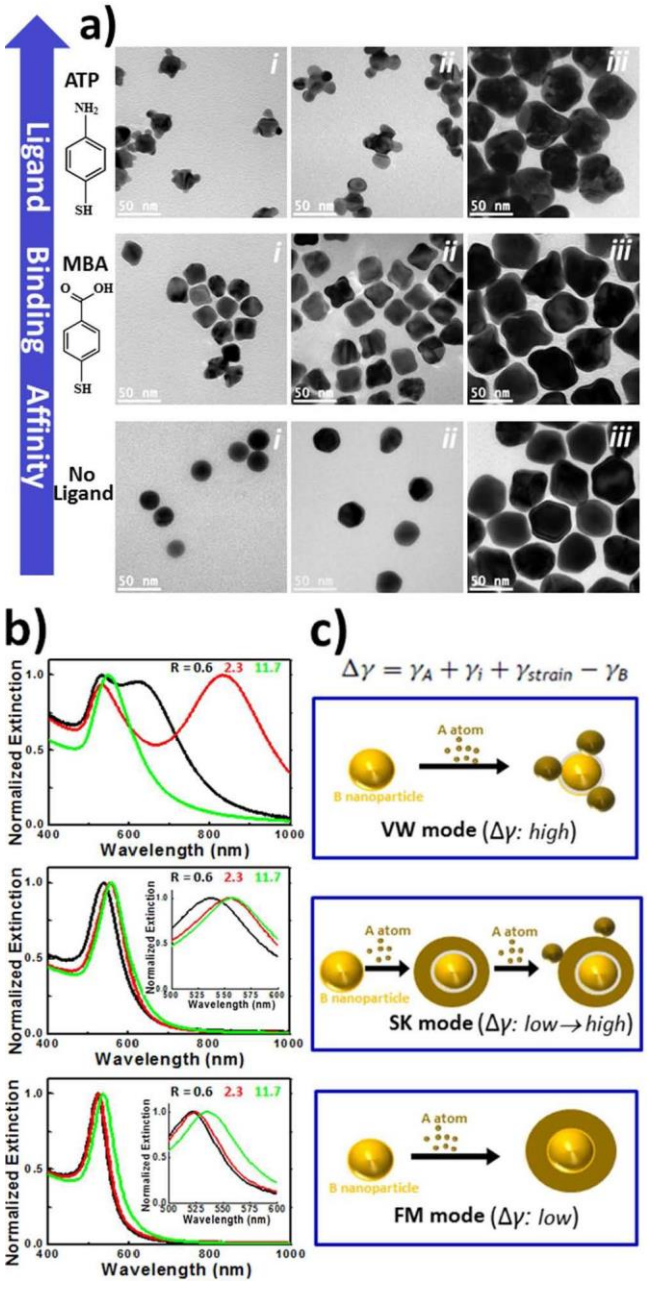

Figure 2. Gold shell growth with different ligands: ATP, MBA, and No Ligand. Synthesis conditions were the same for samples with the same R values: (i) 0.6, (ii) 2.3, (iii) 11.7. a) TEM images, b) UV-Vis spectra, c) schematic illustrations of different crystal growth modes, where the overall excess energy (Δγ) determines the core-shell growth mode (see text for details).

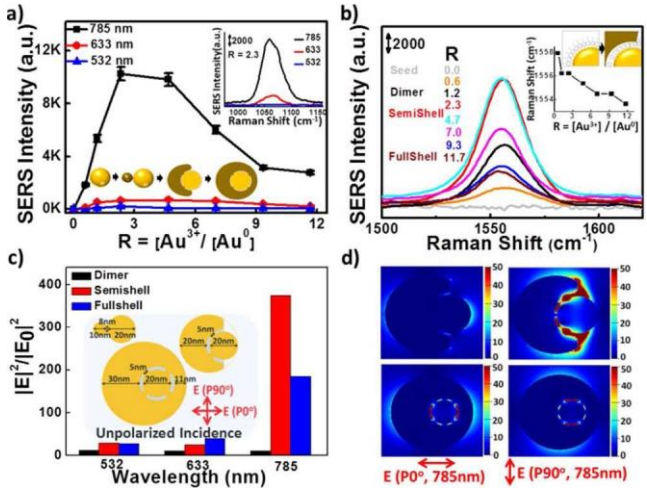

Figure 3. SERS response of plasmonic gold nanostructures. a) SERS intensity of the CH bending mode (1057 cm^{-1}) as a function of R, at different excitation wavelengths (785, 633, and 532 nm). The inset shows SERS bands (R = 2.3, different excitations). b) SERS bands corresponding to the phenyl ring stretching mode (1557 cm^{-1}) from nanostructures grown with different R values, under 785 nm laser excitation. Inset: Raman shift vs. R. c,d) E-field simulation of plasmonic nanostructures: c) Average E-field enhancement for three different nanostructures (dimer, semishell and fullshell) under unpolarized excitation at 532 nm, 633 nm, and 785 nm. The inset shows the geometric models used for the simulations. d) E-field mapping of semishell and full-shell nanostructures under 785 nm excitation with both 0° and 90° polarization as indicated; all scale bars indicate 20 nm. Note that SERS spectra were collected from samples with the same particle concentration and presented after background subtraction.

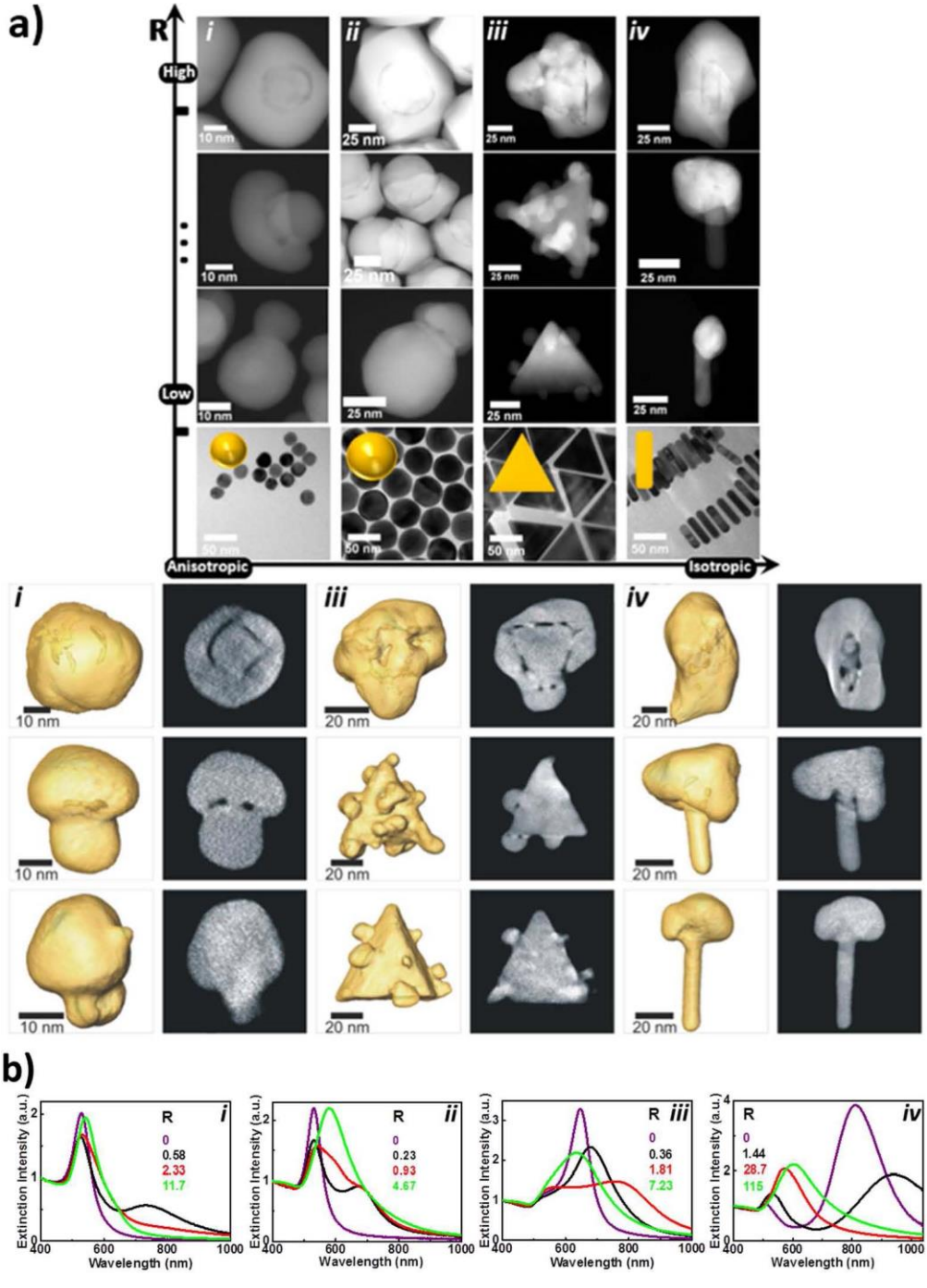

Figure 4. Diversity of the plasmonic nanostructures via ligand-mediated interfacial control. a) Upper panel: HAADF-STEM and TEM images of nanostructures obtained using different nanoparticle seeds including (i) nanospheres (20 nm), (ii) nanospheres (50 nm), (iii) nanotriangles (60 nm * 20 nm), (iv) nanorods (46 nm * 12 nm). Lower panel: 3D TEM and slice images of nanostructures using different nanoparticle seeds. b) Extinction spectra from the same BDT-embedded plasmonic nanostructures with different R values.